Nature Communications

https://doi.org/10.1038/s41467-026-70742-3

Article in Press

Photoinduced radical-mediated atomic dispersion of noble metal nanoparticles

Received: 5 September 2025

Accepted: 5 March 2026

Cite this article as: Chen, X., Zhao, Q., Zhang, J. *et al.* Photoinduced radical-mediated atomic dispersion of noble metal nanoparticles. *Nat Commun* (2026). https://doi.org/10.1038/s41467-026-70742-3

Xiang Chen, Qingfei Zhao, Jingyuan Zhang, Kehan Zhou, Xufang Qian & Zhenfeng Bian

Photoinduced Radical-Mediated Atomic Dispersion of Noble Metal Nanoparticles

Xiang Chen[a], Qingfei Zhao[a], Jingyuan Zhang[a], Kehan Zhou[a], Xufang Qian*[b], Zhenfeng Bian*[a]

[a] X. Chen, Q. Zhao, J. Zhang, K. Zhou, Prof. Z. Bian
MOE Key Laboratory of Resource Chemistry and Shanghai Key Laboratory of Rare Earth Functional Materials, Shanghai Normal University, Shanghai 200234, China
E-mail: bianzhenfeng@shnu.edu.cn

[b] Prof. X. Qian
School of Environmental Science and Engineering, Shanghai Jiao Tong University, Shanghai 200240, China
E-mail: qianxufang@sjtu.edu.cn

Abstract

The transformation of noble metal nanoparticles into atomically dispersed catalysts has been a long-standing goal to enhance metal utilization and regenerate the activity of agglomerated catalysts. Traditional methods, however, often require high temperatures, specific atmospheres, or complex chemical processes. We present a novel photoinduced strategy for atomic dispersion of noble metal nanoparticles under ambient conditions. Experimental and density functional theory calculations reveal that chlorine radicals (•Cl), together with $•O_2^-$, promote Pd-Pd bond cleavage. The intermediate $[PdCl_4]^{2-}$ species formed adsorbs onto TiO_2 via electrostatic interactions and, upon dechlorination, stabilizes into a single-atom Pd_1-N_2O_1 structure. This method is applicable to various noble metals (Pd, Pt, Rh) and different oxide supports (TiO_2 and WO_3), and significantly enhances the

catalytic activity of both commercial Pd/C and industrial waste Pd/C catalysts by 17.8-fold and 26-fold, respectively, in the hydrogenation of styrene. This approach offers a simple, green, and sustainable solution for advancing catalytic technologies.

Introduction

Noble-metal-based catalysts, such as palladium (Pd), platinum (Pt), and rhodium (Rh), are critical in energy conversion[1,2], chemical synthesis[3], and environmental remediation[4] due to their exceptional stability and catalytic performance. However, the scarcity and high cost of these metals necessitate improving their atomic efficiency to reduce production costs and foster the green and sustainable development of related industries[5-7]. Recently, dispersing noble metals into ultra-small forms, such as nanoparticles, clusters, and single atoms, has emerged as an effective strategy to enhance both atomic efficiency and catalytic performance[8-10]. Nanoparticles and single-atom catalysts exhibit differences in chemical states and coordination environments, which leads to distinct catalytic reaction pathways and different catalytic applications. Among these, single-atom catalysts (SACs) have garnered significant attention due to their unique electronic properties and maximized atomic utilization, leading to exceptional catalytic activity[11-14]. Yet, SACs' high surface energy makes them susceptible to sintering into larger nanoparticles under harsh conditions, which can dramatically reduce their catalytic performance and lead to deactivation[15-20].

To address these challenges, various strategies have been developed to achieve atomic dispersion of noble metal nanoparticles. These include atom trapping, in-situ pyrolysis, reaction

induction, and ligand assistance. For instance, Datye et al. achieved single-atom dispersion of Pt on CeO_2 by treating Pt nanoparticle-loaded alumina and CeO_2 mixtures at 800 °C[21]. Wei et al. encapsulated Pd nanoparticles in ZIF-8 and, after pyrolysis at 900 °C, observed Pd coordinated as single atoms with nitrogen[22]. Feng et al. converted Rh nanoparticles into single atoms using a specific atmosphere of N_2 flow and CO/CH_3I at 513 K[23], while Wang et al. employed organic chloride ligands at 400 °C to convert Pd nanoclusters into Pd single atoms[24]. In these approaches, the nanoparticles are first activated by high temperature treatments or reactive atmospheres, which mobilize metal atoms from the particle surface and cleave metal-metal bonds, and the resulting mobile species are then trapped and stabilized as isolated atoms at strong anchoring sites such as defects or heteroatom coordination environments on the support. In particular, atom-trapping and in situ pyrolysis strategies rely on thermally induced migration or volatilization of metal species that are captured by defect sites, whereas reaction induced and ligand assisted strategies use specific reactants or coordinated ligands to weaken metal-metal bonds and promote the stepwise transformation of metal nanoparticles or clusters into isolated single atom centers. Although these methods have made significant strides in overcoming sintering and improving noble metal utilization, they often require high temperatures, specific atmospheres, or complex chemical operations, which can increase energy consumption, production costs, and environmental impacts. Therefore, developing a simple and energy-efficient strategy for converting noble metal nanoparticles into single atoms under mild conditions is crucial for advancing sustainable catalytic technologies.

Here, we propose a novel photoinduced strategy that achieves atomic dispersion of noble

metal nanoparticles under ambient temperature and pressure. Operationally, the dispersion is carried out in an acetonitrile-HCl mixed solution (CH_3CN/HCl, v/v = 1:0.00005) containing nanoparticle and oxide supports, which is simply irradiated with UV light at room temperature, without the need for high temperature calcination or controlled gas atmospheres. This intrinsically reduces energy input and simplifies scale-up. Experimental results and density functional theory (DFT) calculations show that chlorine radicals (•Cl) generated during the reaction reduce the electron density around Pd atoms, weakening the stability of Pd-Pd bonds. This, in combination with the attack by $\bullet O_2^-$, leads to the cleavage of Pd-Pd bonds. The resulting intermediate species, $[PdCl_4]^{2-}$, adsorbs onto the TiO_2 surface through electrostatic interactions, and upon dechlorination, forms a stable single-atom Pd_1-N_2O_1 structure, thus achieving atomic dispersion. This strategy is applicable to a range of noble metals, including Pd, Pt, and Rh, and can be extended to different oxide supports such as TiO_2 and WO_3. Notably, photoinduced treatment significantly enhances the catalytic performance of both commercial and industrial waste Pd/C catalysts in the hydrogenation of styrene. Together, these results highlight both the generality and the scalability of this photoinduced approach.

Results and Discussion

The proposed photoinduced strategy for achieving atomic dispersion of noble metal nanoparticles is illustrated in Figure 1a. At ambient temperature and pressure, Pd_{NPs}/TiO_2 were dispersed in an acetonitrile-HCl solution (volume ratio 1:0.00005), followed by ultraviolet (UV) light irradiation. After 1 hour of exposure to UV light, the Pd_1/TiO_2 product was collected through centrifugation, washing, and drying (see Figure S1). High-angle annular dark-field

scanning transmission electron microscopy (HAADF-STEM) images (Figures 1b and 1c) show that, before UV irradiation, Pd nanoparticles were visibly distributed across the TiO_2 surface. Post-irradiation, however, the Pd nanoparticle structure was no longer observable, indicating a significant morphological transformation.

Energy-dispersive X-ray spectroscopy (EDS) mapping (Figures 1e and 1f) revealed that, after the photoinduced treatment, Pd was still present on the TiO_2 surface, but its distribution had changed from being concentrated within particle regions to a more uniform dispersion. Inductively coupled plasma optical emission spectrometry (ICP-OES) analysis confirmed that the Pd content remained essentially unchanged before and after the UV treatment (Table S1). Further characterization using aberration-corrected HAADF-STEM (Figures 1d, 1g, and S2) showed that Pd atoms exhibited isolated distribution on TiO_2. These results demonstrate that the photoinduced strategy successfully achieved atomic dispersion of Pd nanoparticles.

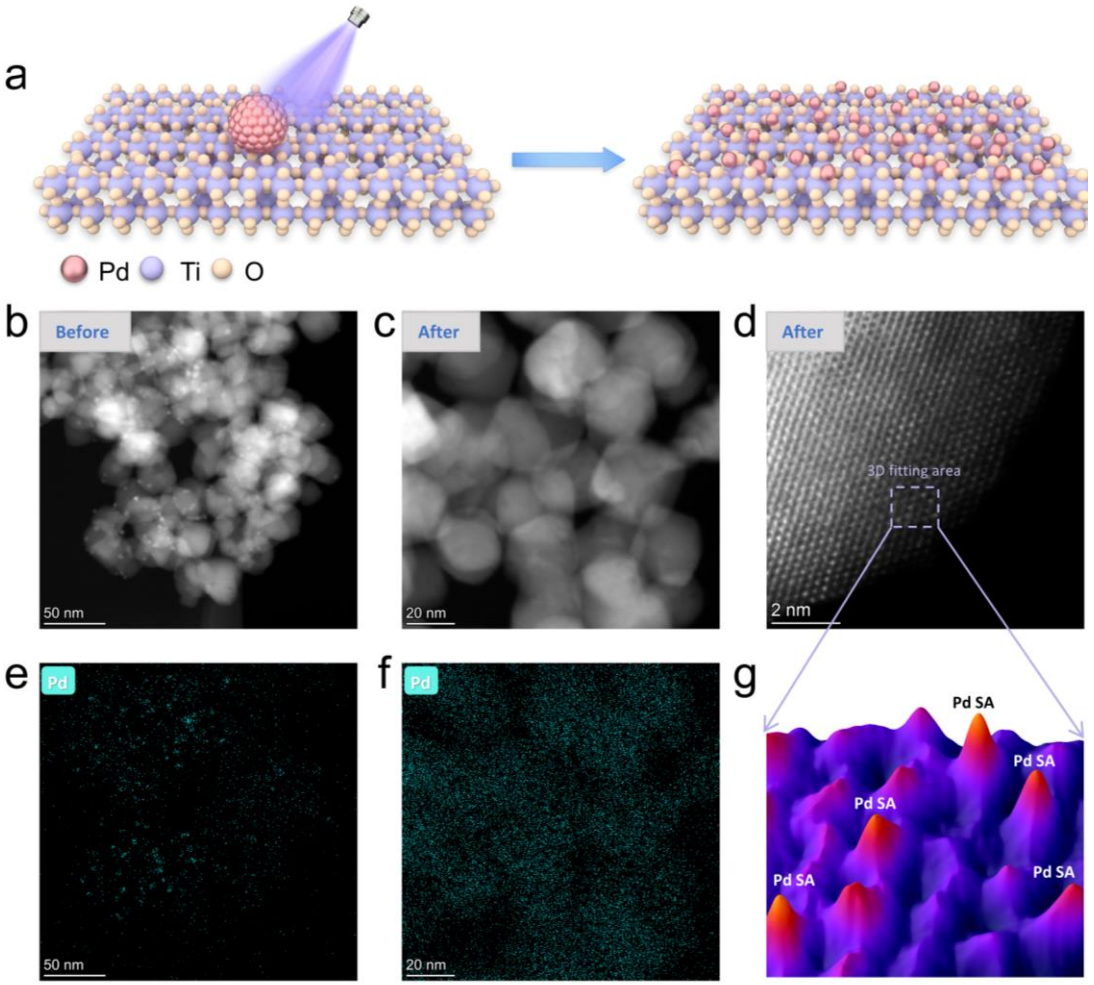

Figure 1. Photoinduced atomic dispersion of Pd nanoparticles. (a) Schematic illustration of the photoinduced conversion of Pd_{NPs}/TiO_2 to Pd_1/TiO_2. HAADF-STEM images of Pd_{NPs}/TiO_2 (b) before and (c) after photoinduced treatment. (d) AC HAADF-STEM image of Pd_1/TiO_2. EDS elemental mapping of Pd_{NPs}/TiO_2 (e) before and (f) after photoinduced treatment. (g) 3D intensity plot of Pd_1/TiO_2.

To investigate the photoinduced atomic dispersion process of Pd nanoparticles (Pd NPs), we subjected Pd_{NPs}/TiO_2 samples to varying light irradiation times. Prior to light exposure, HAADF-STEM images revealed that the average diameter of the Pd NPs was approximately 2.72 nm (Figure 2a, S3). After 15 minutes of irradiation, the average diameter of the Pd particles

decreased to about 2.20 nm, indicating a reduction in particle diameter (Figure 2b, S4). After 30 minutes, the particles further reduced in diameter, forming clusters around 1.33 nm (Figure 2c, S5). After 60 minutes of irradiation, the nanoparticle structure became unobservable, indicating complete conversion into single atoms (Figure 2d, S6). These observations suggest that the Pd NPs gradually reduced in size, ultimately achieving atomic dispersion.

To further explore the photoinduced atomic dispersion of Pd NPs, we employed CO adsorption diffuse reflectance infrared Fourier transform spectroscopy (CO-DRIFTS) to characterize the Pd species (Figures 2e-h). The CO adsorption peaks at ~2170 cm^{-1} and ~2119 cm^{-1} correspond to the R and P branches of gaseous CO, respectively[25]. Before light irradiation (Figure 2e), a distinct absorption peak at 1923 cm^{-1} was observed, indicating that CO was bridged on Pd nanoparticles[26], which confirmed that Pd predominantly existed in nanoparticulate form. As the irradiation time increased, the CO adsorption peaks gradually shifted. After 15 minutes of light exposure (Figure 2f), new peaks appeared at 2085 cm^{-1} and 1948 cm^{-1}, corresponding to CO adsorbed linearly on single atoms and CO bridged on nanoparticles, respectively[27]. This suggests that some Pd NPs were converted into Pd single atoms. After 30 minutes of irradiation (Figure 2g), the CO linear adsorption peak shifts to 2090 cm^{-1}[28], indicating further transformation toward single-atom Pd. After 60 minutes of light irradiation (Figure 2h), the CO adsorption peak appears only at 2160 cm^{-1}, corresponding to CO linearly adsorbed on Pd single atoms[29], indicating complete conversion of Pd NPs into single atoms.

To gain deeper insight into the atomic structural evolution of Pd species, we conducted quasi in-situ X-ray absorption fine structure (XAFS) measurements at the Pd K-edge. The X-ray

absorption near-edge structure (XANES) spectra showed a gradual increase in the white-line intensity with longer irradiation times (Figure S7), suggesting that the oxidation state of Pd increased over time. The XPS spectra of Pd 3*d* further show that, with increasing irradiation time, Pd gradually transforms from Pd^0 (334.81 eV, $3d_{5/2}$) to Pd^{2+} species (337.49 eV, $3d_{5/2}$) (Figure S8). Together, these results indicate that Pd transitioned from a metallic to an oxidized state under light irradiation[30,31], with Pd atoms likely dissociating from nanoparticles and interacting with TiO_2 surface sites.

The Fourier-transformed (FT) k^3-weighted extended X-ray absorption fine structure (EXAFS) spectra for Pd/TiO_2 at various irradiation times are presented in Figures 2i-l. The characteristic peaks at approximately 1.5 Å and 2.5 Å correspond to Pd-N/O and Pd-Pd coordination shells, respectively[32]. With increasing irradiation time, the intensity of the Pd-Pd peak gradually decreased and eventually disappeared, while the Pd-N/O peak intensified. This shift indicates the photoinduced dispersion of Pd NPs into single-atom structures, which bind to N/O sites on TiO_2. Notably, during the intermediate irradiation stages, a Pd-Cl peak around 2.0 Å emerged (Figures 2j-k)[24], suggesting that chloride species may promote Pd atom dissociation from the nanoparticles, aiding the formation of single atoms.

Wavelet transform (WT) contour plots for Pd/TiO_2 samples at different irradiation times (Figures 2m-p) show that at the initial stage (0 minutes), the maximum intensity at approximately 9.0 $Å^{-1}$ corresponds to Pd-Pd coordination, confirming that Pd was predominantly in nanoparticle form. As the irradiation time increased, the Pd-Pd bond signal gradually weakened and disappeared, while the signal for Pd-O/N bonds at around 4.5 $Å^{-1}$ gradually

appeared and strengthened[33]. This change further supports the transition of Pd from nanoparticles to single-atom structures. Quantitative structural analysis through least-squares EXAFS curve fitting (Table S2, Figures S9-10) revealed that initially, Pd existed as nanoparticles with a Pd-Pd coordination number of 9.8. As irradiation progressed, the Pd-Pd coordination number decreased, while the Pd-O/N and Pd-Cl coordination numbers increased, indicating the dispersion of Pd NPs with chloride involvement. After 60 minutes of irradiation, the Pd-Pd and Pd-Cl coordination numbers completely disappeared, and only Pd-O/N coordination remained, with a coordination number of 3. This confirms that Pd NPs were fully dispersed into single atoms, where the Pd single atoms coordinate with three N/O atoms on the TiO_2 surface, forming a stable Pd_1-N_2O_1 structure (Figure 2l, S2, S11, S23).

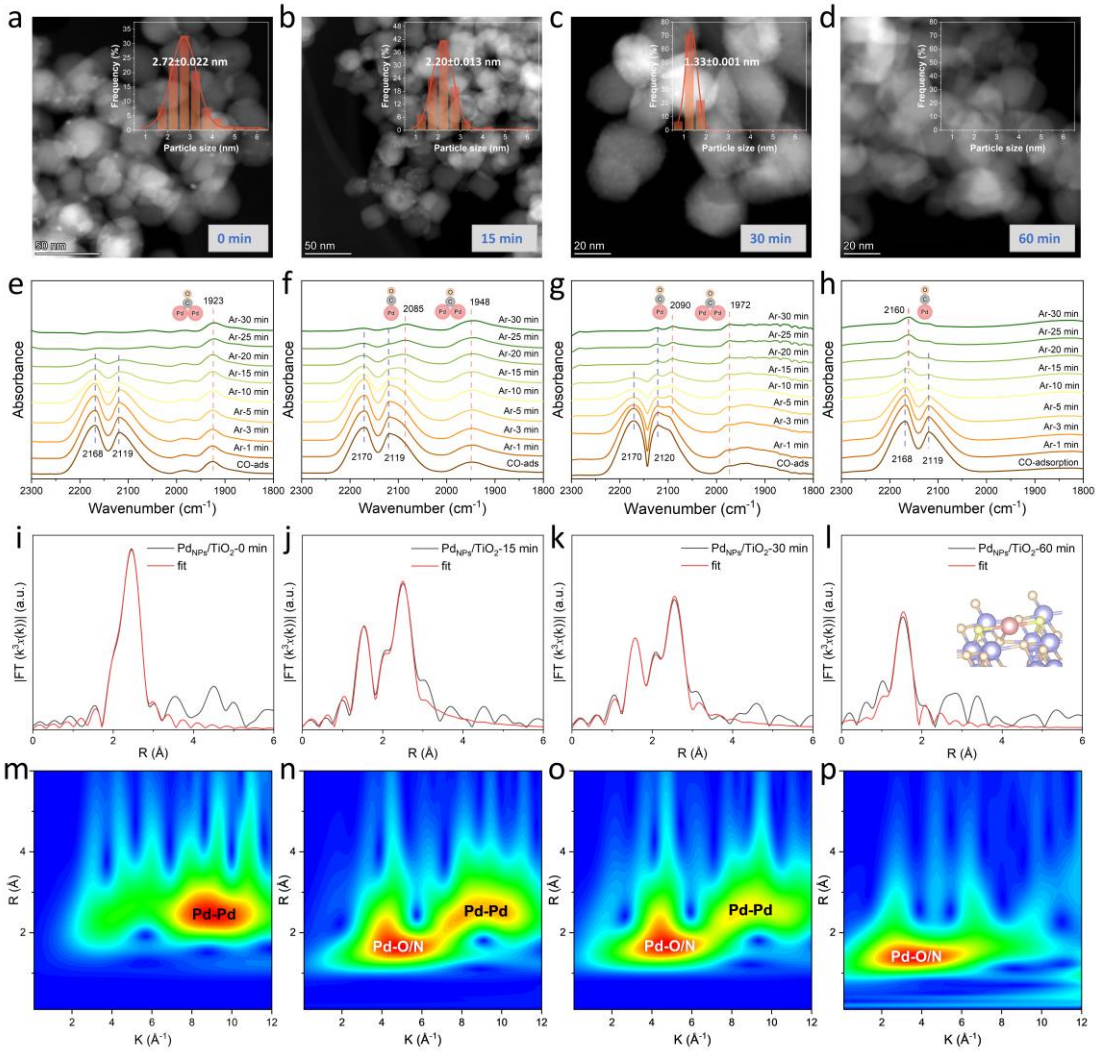

Figure 2. Photoinduced transformation of Pd_{NPs}/TiO_2 to Pd_1/TiO_2. (a)-(d) HAADF-STEM images and Pd particle diameter distributions of Pd_{NPs}/TiO_2 after photoinduced treatment for 0, 15, 30, and 60 minutes, respectively. The number of Pd particle counted was 274, 139 and 172 for 0, 15 and 30 minutes, respectively. (e)-(h) DRIFTS spectra of CO adsorption at saturation coverage and followed by Ar flushing on Pd_{NPs}/TiO_2 after photoinduced treatment for 0, 15, 30, and 60 minutes, respectively. (i)-(l) Fourier transforms of the Pd K-edge EXAFS spectra of Pd_{NPs}/TiO_2 after photoinduced treatment for 0, 15, 30, and 60 minutes, respectively. The inset in Figure 2i shows the corresponding structural model, with Pd (pink), N (light yellow), O (light orange) and Ti (purple). (m)-(p) Wavelet transform of Pd_{NPs}/TiO_2 after photoinduced treatment for 0, 15, 30, and 60 minutes, respectively.

In previous characterizations, such as HAADF-STEM, CO-DRIFTS, and XAFS, we observed that under UV light irradiation, the Pd-Pd bonds in Pd_{NPs}/TiO_2 gradually transformed into Pd-O/N bonds of single-atom Pd. To gain deeper insight into this phenomenon and uncover its detailed mechanism, we designed a series of control experiments to investigate the roles of UV light, acetonitrile, chloride ions, and oxygen in the transformation of Pd nanoparticles into single atoms.

The HAADF-STEM results (Figures 3a-d and S12-S15) reveal that, in the absence of UV light, the average diameter of Pd NPs remains stable at 2.72 nm, indicating that UV light irradiation is essential for the atomic dispersion of Pd NPs. Under aqueous conditions, the average diameter of Pd NPs increased to 3.76 nm. In the absence of chloride ions, the average particle diameter was 3.0 nm, while in an oxygen-free environment, the average diameter was reduced to 2.62 nm. ICP analysis (Table S3) showed that the Pd loading did not undergo significant changes under these control conditions. These results confirm that UV light, acetonitrile, chloride ions, and oxygen are critical factors in the photoinduced conversion of Pd NPs to single atoms.

Having identified these key factors, we further investigated their specific roles in the photoinduced transformation of Pd NPs. During the photoinduced process, TiO_2, as a semiconductor, generates electron-hole pairs upon UV excitation (Equation 1) (Figure S16)[34]. These electrons and holes migrate to the catalyst surface, where the electrons react with oxygen to form superoxide radicals ($\bullet O_2^-$) (Equation 2)[35], while the holes react with acetonitrile and chloride ions, respectively, generating alkyl radicals ($\bullet CH_2CN$) (Equation 3)[36] and chlorine

radicals (•Cl) (Equation 4)[37]. The reactions are as follows:

$$TiO_2 \rightarrow e^- + h^+ \quad (1)$$

$$O_2 + e^- \rightarrow \cdot O_2^- \quad (2)$$

$$CH_3CN + h^+ \rightarrow \cdot CH_2CN + H^+ \quad (3)$$

$$Cl^- + h^+ \rightarrow \cdot Cl \quad (4)$$

Electron paramagnetic resonance (EPR) spectroscopy (Figures 3e-g) confirmed the formation of •Cl, $\bullet O_2^-$, and $\bullet CH_2CN$ under UV irradiation, while no significant EPR signals were observed under dark conditions. This indicates that UV light irradiation triggers the formation of these active species on the TiO_2 surface.

To further explore the roles of these active species in the photoinduced transformation of Pd NPs, we used p-benzoquinone, 2,3-dicyano-5,6-dichlorobenzoquinone (DDQ), and methanol to capture $\bullet O_2^-$, electrons (e^-), and holes (h^+), respectively (Figures 3h-i, S17-S19, and Table S4)[36]. Experimental results showed that when $\bullet O_2^-$ was captured, Pd particles still existed, with an average diameter of 1.75 nm, and the Pd loading did not significantly change, indicating that $\bullet O_2^-$ facilitated the cleavage of Pd-Pd bonds. When electrons were captured, Pd particles still existed, with an average diameter of 1.64 nm, but the Pd loading decreased. According to Equation 2, capturing electrons inhibits the generation of $\bullet O_2^-$, further confirming the key role of $\bullet O_2^-$ in Pd-Pd bond cleavage. The decrease in Pd loading suggests that electrons may also play a role in the formation of Pd single atoms on TiO_2. Capturing electrons may interfere with the electron

transfer between Pd intermediates and TiO_2, affecting the anchoring of Pd single atoms and thus reducing Pd loading. When holes (h^+) were captured, Pd particles still existed (Figure S19), with an average diameter of 2.47 nm, and the Pd loading did not significantly change. According to Equation 4, capturing h^+ inhibited the generation of •Cl, highlighting the crucial role of •Cl in the Pd-Pd bond cleavage process.

Furthermore, through UV-vis spectroscopy, we successfully detected the reaction intermediate species $[PdCl_4]^{2-}$ (Figure 3j)[38]. Zeta potential measurements of TiO_2 in acetonitrile showed that TiO_2 has a positive surface potential (Figure 3k), indicating that the intermediate $[PdCl_4]^{2-}$ ions can adsorb onto the TiO_2 surface through electrostatic interactions (Figure S20)[39]. According to the literature, once $[PdCl_4]^{2-}$ ions adsorb onto the TiO_2 surface, each ion releases two Cl^- ligands, forming a single $PdCl_2$ unit on the TiO_2 surface[39]. Subsequently, the $•CH_2CN$ radicals react with the $PdCl_2$ unit[32], removing chlorine and ultimately, through the combined action of nitrogen atoms and lattice oxygen on TiO_2, anchoring the Pd single atom on the TiO_2 surface, forming a stable Pd_1-N_2O_1 structure (Figure 2l, S2, S11, S23)[40].

Based on these experimental findings, we propose a mechanism for the photoinduced atomic dispersion of Pd NPs, as depicted in Figure 3l. This process can be divided into two key steps: (1) Pd-Pd bond cleavage: The •Cl and $•O_2^-$ radicals generated by UV light excitation, along with chloride ions, cooperate to break the Pd-Pd bonds, generating the intermediate $[PdCl_4]^{2-}$. (2) Pd single atom formation: The intermediate $[PdCl_4]^{2-}$ adsorbs onto the TiO_2 surface via electrostatic interactions and releases two chloride ions, forming a $PdCl_2$ unit. The $•CH_2CN$ radicals then react with the $PdCl_2$ unit, removing the chloride ions and ultimately anchoring the

Pd single atom at the N sites on the TiO_2 surface, forming a stable Pd_1-N_2O_1 structure. During this process, the radicals in the solution and the removed chloride ions continue to interact with the remaining Pd-Pd bonds, until all Pd-Pd bonds are converted to Pd-N/O bonds, achieving complete atomic dispersion of Pd NPs.

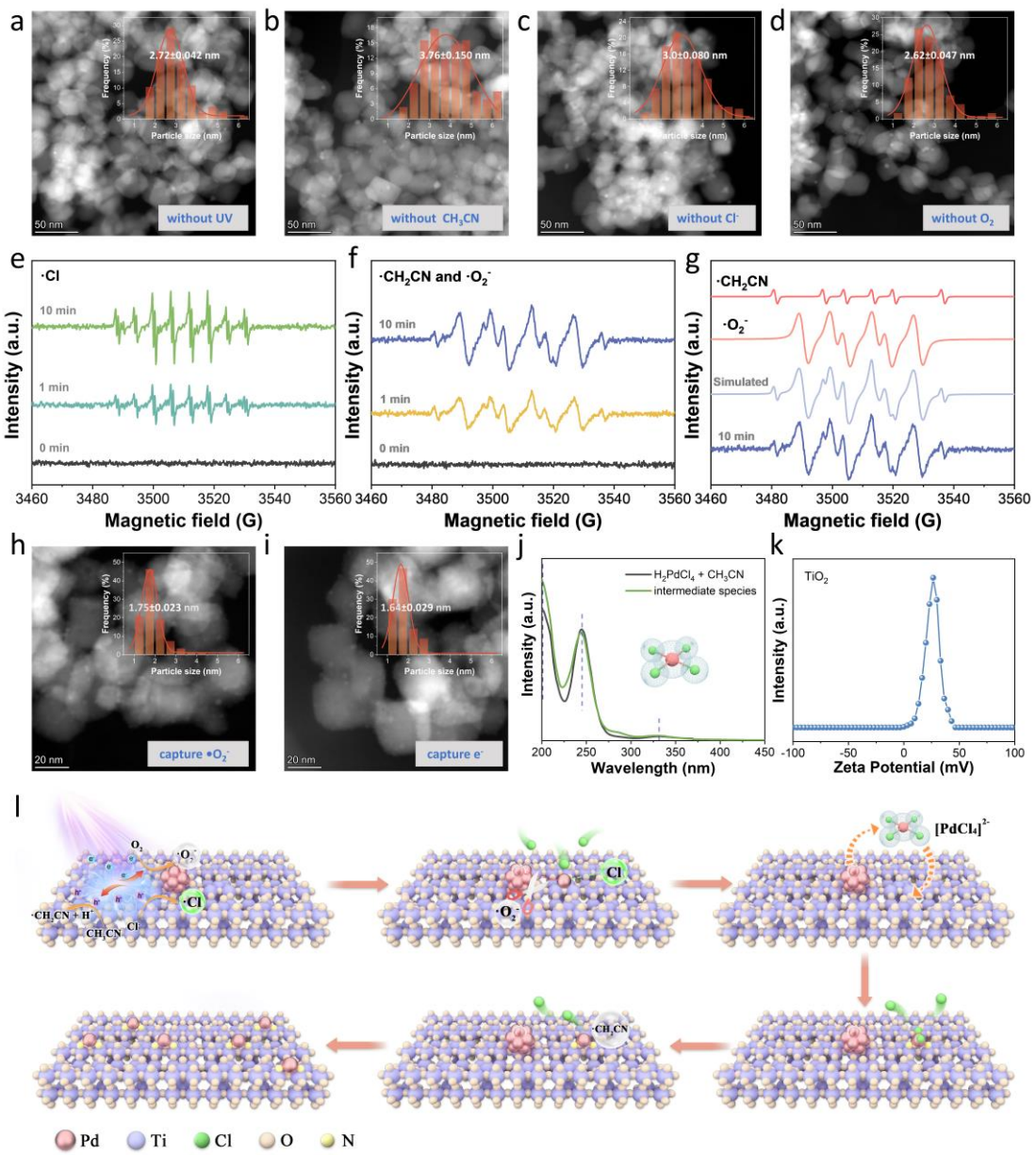

Figure 3. Mechanism of photoinduced atomic dispersion of Pd NPs. HAADF-STEM images and Pd particle diameter distributions of Pd_{NPs}/TiO_2 after photoinduced treatment under the following

conditions: (a) without UV light, (b) without CH_3CN, (c) without Cl^-, and (d) without O_2. The number of Pd particles counted was 205, 133, 204 and 115, respectively. (e) chlorine radicals, (f)-(g) superoxide radicals and alkyl radicals generated during the photoinduced transformation of Pd_{NPs}/TiO_2 to Pd_1/TiO_2. HAADF-STEM images and Pd particle diameter distributions of Pd_{NPs}/TiO_2 after photoinduced treatment under the following conditions: (h) capture of $\bullet O_2^-$ and (i) capture of electrons (e^-). The number of Pd particles counted was 302 and 150, respectively. (j) UV-vis spectra of Pd intermediate species. (k) Zeta potential of TiO_2 dispersed in CH_3CN. (l) Schematic illustration of the mechanism for the photoinduced transformation of Pd_{NPs}/TiO_2 to Pd_1/TiO_2.

To further elucidate the mechanism underlying the transformation of Pd NPs to Pd single atoms, we performed density functional theory (DFT) calculations to simulate the interactions between free radicals and Pd NPs, as well as the formation of Pd single atoms (Figure 4). For simplicity, a small nanoparticle consisting of 12 Pd atoms (Pd_{12}) was chosen as the model for Pd NPs, and an anatase TiO_2 (101) facet with N sites was used as the support.

First, we simulated the effect of •Cl on the Pd-Pd bond cleavage process. The DFT calculation results show that after •Cl radicals adsorb onto the Pd atoms at the surface of Pd NPs, the Pd-Pd bond length increases, and the bond energy decreases (Figure 4, I-II and Figure S21). The free energy change for this process is significantly negative (ΔG = -3.51 eV), indicating that the adsorption of •Cl is thermodynamically favorable. Additionally, the charge density difference calculation (Figure S22) reveals that •Cl adsorption reduces the electron density around the Pd atoms, thereby weakening the stability of the Pd-Pd bond. Subsequently, $\bullet O_2^-$ attacks the same Pd atom, cooperating with •Cl to further weaken the Pd-Pd bond, ultimately leading to bond cleavage. Meanwhile, Cl^- in the solution coordinates with the cleaved Pd atom, forming the

intermediate product $[PdCl_4]^{2-}$ (Figure 4, II-III). The entire Pd-Pd bond cleavage process (Figure 4, I-III) releases 0.61 eV of energy, indicating that this process is thermodynamically spontaneous. Notably, in the absence of •Cl, the Pd-Pd bond cleavage is endergonic (ΔG = 6.03 eV, Path I-III in Figure 4), highlighting the crucial role of •Cl in Pd-Pd bond cleavage.

Next, the intermediate product $[PdCl_4]^{2-}$ adsorbs onto the TiO_2 surface and releases two Cl^- ions, forming the adsorption structure of a single $PdCl_2$ unit (Figure 4, III-IV). This adsorption structure corresponds to a Pd-N_2Cl_2 coordination environment. COHP analysis (Figure S23) shows that the Pd-N bonds exhibit stronger bonding interactions than the Pd-Cl bonds, supporting the stabilization and N-site anchoring of the adsorbed intermediate. The calculation results show that this adsorption process releases 0.84 eV of energy, suggesting that the adsorption of the intermediate product is thermodynamically favorable. Given the high reactivity of •CH_2CN, these radicals readily react with the adsorbed $PdCl_2$ unit to remove chloride. Our calculations further show that the $PdCl_2$ unit progressively dechlorinates, ultimately forming Pd single atoms that are anchored at N sites on the TiO_2 surface, resulting in a stable Pd_1-N_2O_1 structure (Figure 4, IV-VI and Figure S23). The formation of Pd single atoms (Figure 4, III-VI) releases 0.8 eV of energy.

Considering the entire reaction pathway, the overall free energy change from Pd-Pd bond cleavage to Pd single atom formation (Figure 4, I-VI) is ΔG = -1.41 eV, indicating that this reaction pathway is thermodynamically highly favorable.

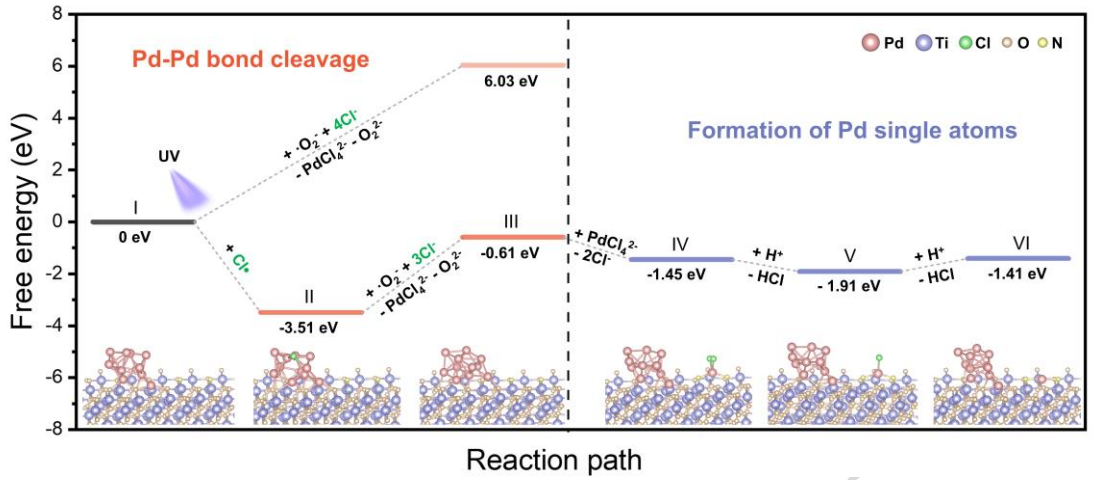

Figure 4. Energies and optimized structures of the Pd-Pd bond cleavage process and the formation of Pd single atoms on TiO_2. (I) The initial state, where Pd nanoparticles are supported on TiO_2. (I-II) The adsorption of •Cl radicals onto Pd nanoparticles. (II-III) The attack of $•O_2^-$ radicals cooperates with •Cl, leading to Pd-Pd bond cleavage and the formation of the intermediate $[PdCl_4]^{2-}$ species. (III-IV) The intermediate adsorbs onto the TiO_2 surface, releasing two Cl^- ions and forming the $PdCl_2$ unit. (IV-VI) The $PdCl_2$ unit progressively dechlorinates, ultimately forming a stable Pd_1-N_2O_1 structure.

To assess the universality of the photoinduced strategy, we applied it to TiO_2 supports with varying particle sizes and to different noble metal nanoparticles. TiO_2-S, with a particle diameter of approximately 2~5 nm, was used as a support to investigate the photoinduced atomic dispersion effects of Pd NPs, Pt NPs, and Rh NPs. HAADF-STEM images revealed that, prior to light irradiation, the diameter of Pd NPs was approximately 3.43 nm (Figure 5a and Figure S24). After irradiation, the Pd NP structure was no longer visible, and EDS analysis indicated that the Pd signal was uniformly distributed across the TiO_2 surface (Figure 5b and Figure S25). CO-DRIFTS spectra (Figure 5c and Figure 5d) show that before light irradiation, an absorption peak at 1972 cm^{-1} was observed, corresponding to CO bridged on nanoparticles[26], suggesting

that Pd predominantly existed as nanoparticles. After light irradiation, the CO adsorption peak appears only at 2160 cm^{-1}, attributed to CO linearly adsorbed on Pd single atoms[29], confirming the transformation of Pd NPs into single atoms.

A similar transformation was observed for Pt NPs and Rh NPs under photoinduced treatment. Prior to light irradiation, the Pt NPs were approximately 2.43 nm in diameter (Figure 5e and S26), and after irradiation, the Pt NPs disappeared, with EDS showing uniform Pt distribution on the TiO_2 surface (Figure 5f and S27). CO-DRIFTS (Figure 5g and Figure 5h) indicated a peak at 1839 cm^{-1} before irradiation, consistent with CO bridged on Pt nanoparticles[9]. After irradiation, the CO adsorption peak appears only at 2090 cm^{-1}, associated with CO linearly adsorbed on Pt single atoms[41], confirming the transformation of Pt NPs to single atoms. Similarly, Rh NPs, which were approximately 1.78 nm in diameter before irradiation (Figure 5i and S28), exhibited complete dispersion after irradiation, with Rh uniformly distributed on the TiO_2 surface (Figure 5j and S29). CO-DRIFTS (Figure 5k and Figure 5l) showed a peak at 1873 cm^{-1} before light irradiation, consistent with CO bridged on Rh nanoparticles[42]. After light irradiation, two peaks appeared at 2085 and 2015 cm^{-1}, corresponding to the symmetric and asymmetric stretching vibrations of $Rh(CO)_2$ gem-dicarbonyl species at Rh single atom sites[43], further confirming the conversion of Rh NPs into single atoms.

To further extend the support scope, we applied the photoinduced strategy to WO_3. For Pd_{NPs}/WO_3, HAADF-STEM and EDS mapping, together with CO-DRIFTS, confirm the conversion of Pd nanoparticles to atomically dispersed Pd species after irradiation (Figure S30). In addition, larger Pd nanoparticles prepared by chemical reduction and subsequently loaded

onto TiO_2 (Pd_{NPs}-CR/TiO_2) were also tested under prolonged UV irradiation using the photoinduced strategy. HAADF-STEM/EDS mapping and CO-DRIFTS confirm the conversion of these Pd nanoparticles into atomically dispersed Pd species (Figure S31). These results demonstrate the broad applicability of the photoinduced strategy to different oxide supports (TiO_2 and WO_3) and diverse noble metal nanoparticles (Pd, Pt, and Rh), highlighting the universality of this approach.

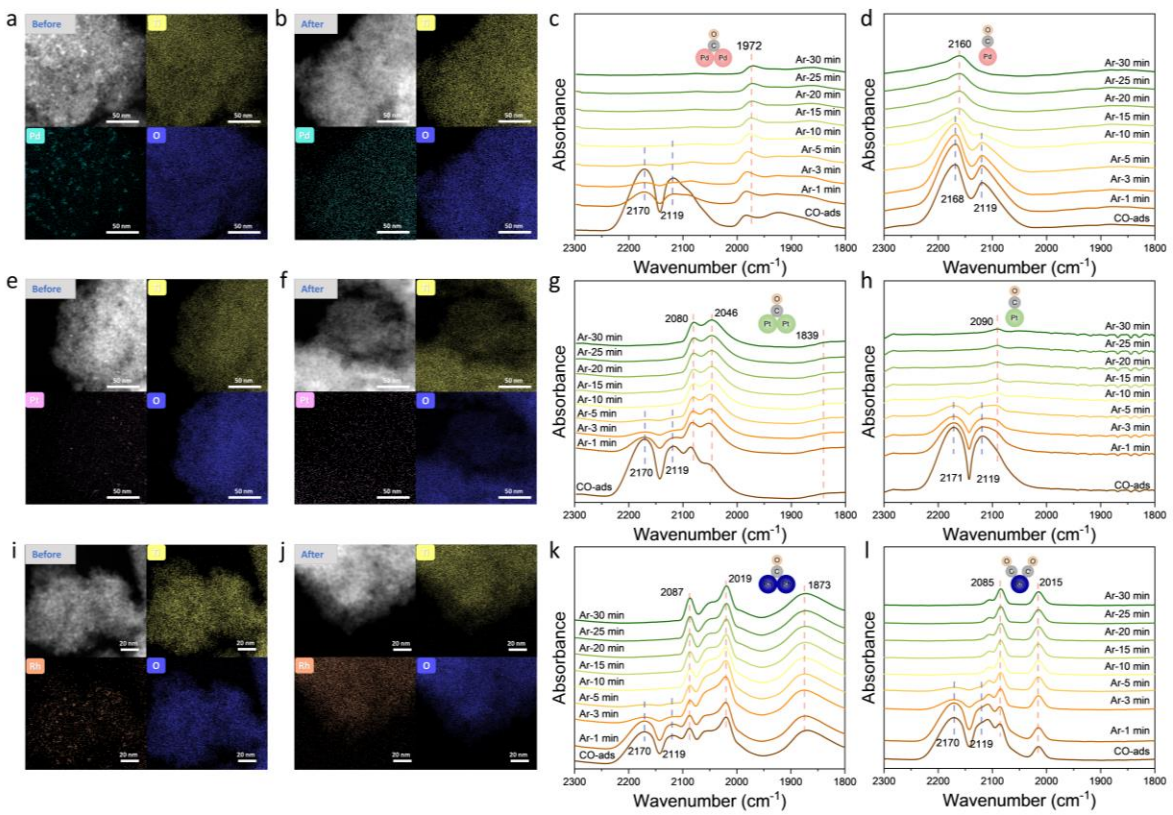

Figure 5. Generality of the photoinduced atomic dispersion strategy. HAADF-STEM images and EDS elemental mappings of Pd_{NPs}/TiO_2 (a) before and (b) after photoinduced treatment, respectively. DRIFTS spectra of CO adsorption at saturation coverage and followed by Ar flushing on Pd_{NPs}/TiO_2 (c) before and (d) after photoinduced treatment, respectively. HAADF-STEM images and EDS elemental mappings of Pt_{NPs}/TiO_2 (e) before and (f) after photoinduced treatment, respectively. DRIFTS spectra of CO adsorption at saturation coverage

and followed by Ar flushing on Pt_{NPs}/TiO_2 (g) before and (h) after photoinduced treatment, respectively. HAADF-STEM images and EDS elemental mappings of Rh_{NPs}/TiO_2 (i) before and (j) after photoinduced treatment, respectively. DRIFTS spectra of CO adsorption at saturation coverage and followed by Ar flushing on Rh_{NPs}/TiO_2 (k) before and (l) after photoinduced treatment, respectively.

The photoinduced atomic dispersion strategy shows immense potential in enhancing and regenerating the performance of industrial catalysts. Our research further validates the effectiveness of this strategy in improving and regenerating the performance of commercial Pd/C (Comm. Pd/C) and industrial waste Pd/C (Ind. W. Pd/C) catalysts. By applying this strategy to these catalysts, we observed atomic dispersion of Pd NPs under photoinduced conditions, as confirmed by HRTEM and CO-DRIFTS characterization (Figures S32-S33). This structural transformation significantly increases the exposure of Pd atoms. In the hydrogenation of styrene, the photoinduced treated commercial Pd/C catalyst [$Pd_1/C\&TiO_2$(Comm.)] and industrial waste Pd/C catalyst [$Pd_1/C\&TiO_2$(Ind.W.)] exhibited remarkable performance improvements (Figures 6a and 6b). Specifically, compared to untreated catalysts (Comm. Pd/C and Ind. W. Pd/C), the catalytic activity of $Pd_1/C\&TiO_2$(Comm.) and $Pd_1/C\&TiO_2$(Ind.W.) increased by 17.8 and 26 times, respectively. Additionally, the TOF values of the photoinduced treated catalysts showed significant improvement (Figure 6c), with the TOF values of $Pd_1/C\&TiO_2$(Comm.) and $Pd_1/C\&TiO_2$(Ind.W.) reaching 8933 h^{-1} and 7067 h^{-1}, respectively—an increase of 8.2 and 8.5 times compared to Comm. Pd/C (1088 h^{-1}) and Ind. W. Pd/C (828 h^{-1}). Notably, both $Pd_1/C\&TiO_2$(Comm.) and $Pd_1/C\&TiO_2$(Ind.W.) maintained nearly 100% conversion after 5 reaction cycles (Figure 6d), demonstrating excellent stability and reusability.

By gaining a deeper understanding of the microscopic mechanism behind the photoinduced nanoparticle atomic dispersion strategy, we aim to apply this approach on a larger scale using continuous flow reactors to regenerate and improve industrial catalysts (Figure 6e and S34). This method successfully achieved atomic dispersion of Pd NPs and enhanced catalytic performance on Ind. W. Pd/C under mild conditions (Figure S35). Notably, we also explored using sunlight as a light source, which successfully facilitated the atomic dispersion of Pd NPs on Pd_{NPs}/TiO_2, further enhancing the catalytic performance of Pd_{NPs}/TiO_2 (Figure S36).

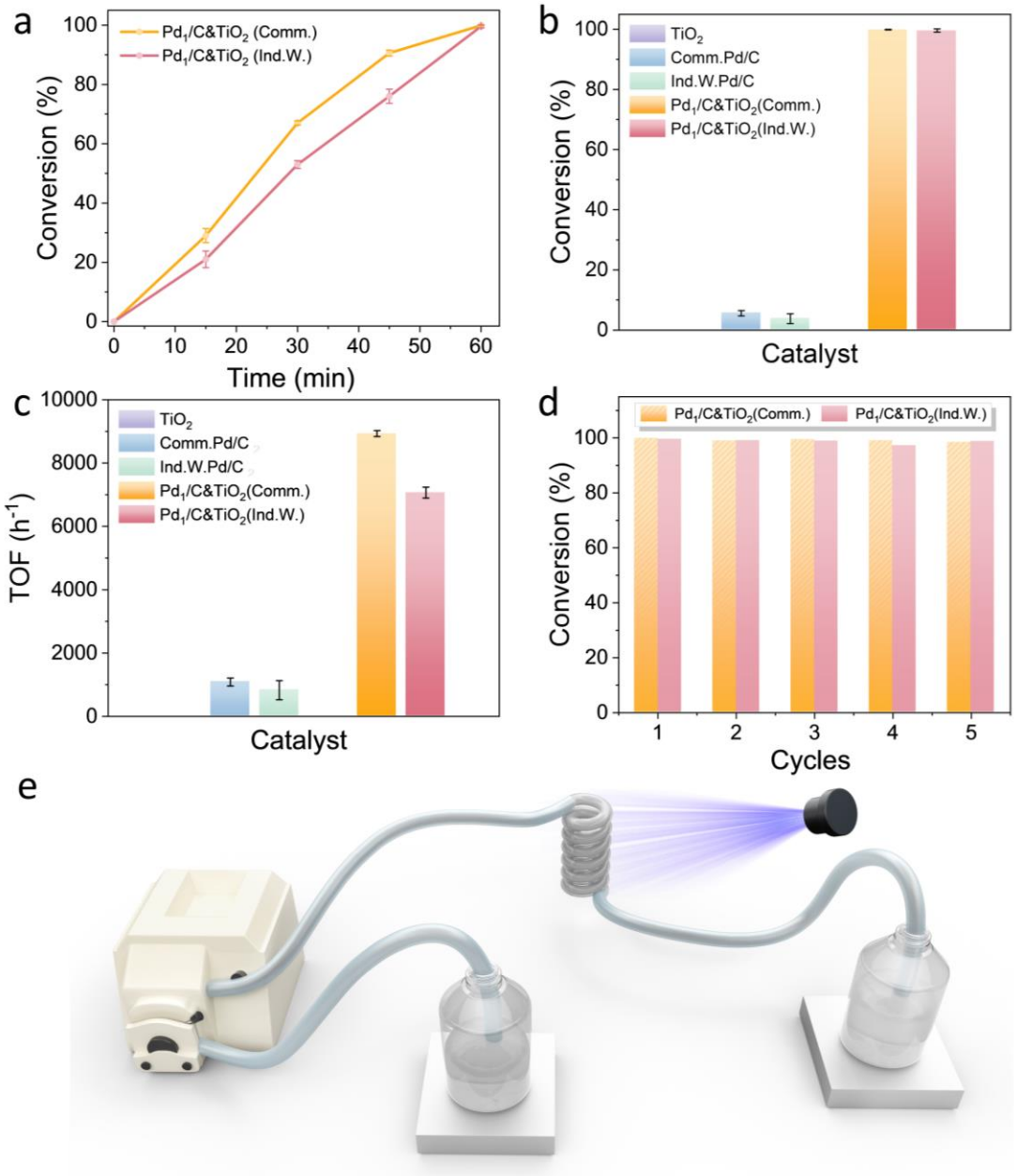

Figure 6. Practical applications of the photoinduced strategy. (a) Catalytic performance of $Pd_1/C\&TiO_2$(Comm.) and $Pd_1/C\&TiO_2$(Ind.W.) in styrene hydrogenation over time. (b) Comparison of catalytic performance of TiO_2, Comm. Pd/C, Ind. W. Pd/C, $Pd_1/C\&TiO_2$(Comm.), and $Pd_1/C\&TiO_2$(Ind.W.) in styrene hydrogenation. (c) Turnover frequency (TOF) (h^{-1}) for styrene hydrogenation reactions catalyzed by the materials shown in (b). (d) Cyclic performance of $Pd_1/C\&TiO_2$(Comm.) and $Pd_1/C\&TiO_2$(Ind.W.) for styrene hydrogenation reactions. (e) Schematic illustration of the photoinduced atomic dispersion process using a continuous flow

reactor. Error bars represent the mean ± s.d. from three independent experiments (n = 3).

Discussion

In conclusion, we introduce a groundbreaking photoinduced strategy for achieving the atomic dispersion of noble metal nanoparticles at ambient temperature and pressure. By leveraging advanced techniques such as STEM, CO-DRIFTS, EXAFS, and DFT calculations, we provide detailed insights into the microscopic mechanisms underpinning this novel dispersion process. Our experimental findings demonstrate the broad applicability of this strategy to a range of noble metals, including Pd, Pt, and Rh, and to different oxide supports such as TiO_2 and WO_3. Notably, the catalytic performance of commercial Pd/C and industrial waste Pd/C catalysts, after photoinduced treatment, exhibited remarkable enhancements in the styrene hydrogenation reaction. This highlights the immense potential of the strategy for the modification and regeneration of industrial catalysts. These results offer valuable perspectives for the efficient use and sustainable development of noble-metal-based catalysts. Moving forward, we aim to expand the applicability of this strategy to other metals and support systems, while assessing its long-term effectiveness and economic viability in industrial applications.

Methods

Chemicals

Titanium oxide (TiO_2) in two forms was used: TiO_2-L (particle diameter ~25 nm, anatase, 99.8%) and TiO_2-S (particle diameter approximately 2~5 nm, anatase, 99%).

Other chemicals included acetonitrile (CH_3CN, HPLC, 99.9%), 2,3-dicyano-5,6-dichlorobenzoquinone (DDQ, AR, 98%), methanol (CH_3OH, GR, ≥99.7%), p-benzoquinone ($C_6H_4O_2$, RG, 99%), hydrochloric acid (HCl, AR, 36-38%), styrene ($C_6H_5CH=CH_2$, 99%), ethanol (C_2H_5OH, HPLC, 99.9%), ethylbenzene ($C_6H_5C_2H_5$, 99%), dimethylformamide (DMF, AR, ≥99.5%), hydrogen (H_2, 99.999%), palladium chloride ($PdCl_2$, 99.9%), chloroplatinic acid hexahydrate ($H_2PtCl_6 \cdot 6H_2O$, RG, 99.9%), rhodium(III) chloride hydrate ($RhCl_3 \cdot xH_2O$, RG, 99%), Tungsten(VI) oxide (WO_3, 99.95%), potassium iodide (KI, AR, 99%), polyvinylpyrrolidone (PVP, M_w ~55,000), sodium tetrachloropalladate (Na_2PdCl_4, 99%), formamide ($HCONH_2$, AR, ≥99.5%), and acetone (AR, 99.5%).

Commercial Pd/C (Comm.Pd/C) with a palladium loading of 5 wt.% was purchased from Adamas-beta (Shanghai, China). Industrial waste Pd/C (Ind.W.Pd/C) with a palladium loading of 10 wt.% was collected after long-term industrial use in hydrogenation reactions. All the chemicals were used as received.

Two different supports, TiO_2-L and TiO_2-S, were used in this study. Among them, TiO_2-L has a particle diameter of approximately 25 nm. As a support, its HAADF-STEM characterization results are relatively clear, enabling more accurate statistical analysis of the diameter distribution of Pd NPs and in-depth exploration of the atomic dispersion mechanism of Pd NPs under photoinduced. On the other hand, TiO_2-S has a smaller particle diameter (approximately 2~5 nm) and a larger specific surface area, which provides favorable conditions for studying the universality and practical applications of photoinduced strategy.

Characterization

High-angle annular dark-field scanning transmission electron microscopy (HAADF-STEM) images and energy dispersive X-ray spectroscopy (EDS) elemental mapping were collected on TALOS F200S. Aberration-corrected high-angle annular dark-field scanning transmission electron microscopy (AC HAADF-STEM) analysis was performed on ThemisZ transmission electron microscope (accelerating voltage, 300 kV). The contents of metal on the catalysts were analyzed by inductively coupled plasma optical emission spectrometer (ICP-OES, EXPEC 6500). The X-ray absorption fine structure spectra (Pd K-edge) were collected at beamline BL44B2 at the SPring-8 synchrotron in Japan. The storage rings of SPring-8 were operated at 8.0 GeV with a maximum current of 250 mA. using Si(111) double-crystal monochromator. All spectra were collected at room temperature. The XAFS spectra were recorded with fluorescence using a 19-element Ge solid-state detector mode. X-ray photoelectron spectroscopy (XPS) data were obtained on Perkin-Elmer PHI 5000. The electron paramagnetic resonance (EPR) spectra of radicals during photoinduced reactions were recorded on a Bruker A300 model spectrometer. The photoinduced reaction intermediate species was investigated using a UV-Vis spectrophotometer (UV-7502, Shimadzu). The zeta potential of the catalysts was measured using a zeta potential analyzer (Malvern Zetasizer Nano ZS). The styrene hydrogenation reaction was analyzed using a gas chromatograph (GC-7890B, Agilent).

DRIFTS for CO adsorption

DRIFTS measurements were performed using a Bruker VERTEX 80v Fourier-transform

spectrometer equipped with a Harrick diffuse reflectance accessory with ZnSe and quartz window. After the sample was loaded into the reaction chamber, pure Ar (99.999%) was purged into the chamber firstly for background spectra collection. Subsequently, CO was introduced into the system until CO adsorbed saturation. Then the pure Ar was purged to remove the gaseous CO and the spectra were collected.

Synthesis of Pd_{NPs}/TiO_2-L

0.25 g of commercial anatase TiO_2-L was dispersed in 50 mL of ethanol in a sealed quartz vial. The TiO_2-L dispersion was purged with Ar gas for 15 minutes. The TiO_2-L dispersion was vigorously stirred and simultaneously irradiated under a 100 W, 360 nm UV lamp for 5 minutes. H_2PdCl_4 solution was diluted to 5 mL using ethanol and then injected into the TiO_2-L dispersion. The mixture was stirred vigorously for an additional 20 minutes. The Pd_{NPs}/TiO_2-L product was collected by centrifugation, washing, and drying. The Pd content in Pd_{NPs}/TiO_2-L was determined to be 0.35 wt.% by ICP analysis. Among them, H_2PdCl_4 is prepared by mixing $PdCl_2$ with HCl.

Synthesis of M_{NPs}/TiO_2-S

100 mg of TiO_2-S was dispersed in 20 mL of ethanol and placed in a quartz bottle, followed by the addition of 3.7 μL of a 1 mol/L H_2PdCl_4 solution. The mixture was vigorously stirred and then sealed with the bottle cap. The uniformly dispersed mixture was irradiated under a 360 nm UV lamp at an intensity of 500 mW/cm² for 0.5 hours. After irradiation, the Pd_{NPs}/TiO_2-S product was collected through centrifugation, washing, and drying. The Pd content in Pd_{NPs}/TiO_2-S was determined to be 0.38 wt.% by ICP analysis. The synthesis of Pt_{NPs}/TiO_2-S and Rh_{NPs}/TiO_2-S followed the same procedure, with $H_2PtCl_6 \cdot 6H_2O$ and H_2RhCl_6 replacing H_2PdCl_4

as the metal precursors, respectively. The Pt content in Pt_{NPs}/TiO_2-S was determined to be 0.36 wt.% by ICP analysis. The Rh content in Rh_{NPs}/TiO_2-S was determined to be 0.37 wt.% by ICP analysis. Among them, H_2PdCl_4 and H_2RhCl_6 are prepared by mixing the corresponding precious metal chlorides with hydrochloric acid.

Synthesis of Pd_{NPs}/WO_3

100 mg of WO_3 was dispersed in 20 mL of ethanol and placed in a quartz bottle, followed by the addition of 2.8 μL of a 1 mol/L H_2PdCl_4 solution. The mixture was vigorously stirred and then sealed with the bottle cap. The uniformly dispersed mixture was irradiated under a 360 nm UV lamp at an intensity of 500 mW/cm^2 for 0.5 h. After irradiation, the Pd_{NPs}/WO_3 product was collected by centrifugation, washing, and drying. The Pd content in Pd_{NPs}/WO_3 was determined to be 0.28 wt.% by ICP analysis.

Synthesis of Pd_1/WO_3

50 mg of Pd_{NPs}/WO_3 was dispersed in 20 mL of CH_3CN and placed in a quartz bottle, followed by the addition of 1 μL of HCl. After placing the cap on the bottle, the mixture was vigorously stirred. The uniformly dispersed mixture was irradiated under a 360 nm UV lamp with an intensity of 500 mW/cm^2 for 2.5 h. After irradiation, the Pd_1/WO_3 product was collected by centrifugation, washing, and drying. ICP analysis determined the Pd content in Pd_1/WO_3 to be 0.26 wt.%.

Synthesis of Pd nanoparticle

34 mg KI and 100 mg PVP (M_w ~55,000) were dissolved in 10 mL formamide and heated to 120 °C. Subsequently, 59 mg of solid Na_2PdCl_4 was added, and the mixture was maintained for

10 min under vigorous stirring. After the reaction, the mixture was cooled to room temperature, 120 mL acetone was added, and the product was collected by centrifugation. The precipitate was washed with acetone by repeated centrifugation. Finally, the obtained Pd nanoparticles were redispersed in 21 mL ethanol.

Synthesis of Pd_{NPs}-CR/TiO_2

500 mg TiO_2-S was dispersed in 5 mL ethanol under stirring to obtain a homogeneous suspension. Subsequently, 1.5 mL of the as-prepared Pd NP dispersion (prepared by the chemical reduction method) was added, and the mixture was stirred for 1 h. The product was collected by centrifugation, washing, and drying. The Pd loading in Pd_{NPs}-CR/TiO_2 was determined to be 0.29 wt% by ICP analysis.

Synthesis of Pd_1-CR/TiO_2

50 mg of Pd_{NPs}-CR/TiO_2 was dispersed in 20 mL of CH_3CN and placed in a quartz bottle, followed by the addition of 1 μL of HCl. After placing the cap on the bottle, the mixture was vigorously stirred. The uniformly dispersed mixture was irradiated under a 360 nm UV lamp with an intensity of 500 mW/cm^2 for 6 h. After irradiation, the Pd_1-CR/TiO_2 product was collected by centrifugation, washing, and drying. ICP analysis determined the Pd content in Pd_1-CR/TiO_2 to be 0.28 wt%.

Synthesis of M_1/TiO_2

50 mg of Pd_{NPs}/TiO_2-L was dispersed in 20 mL of CH_3CN and placed in a quartz bottle, followed by the addition of 1 μL of HCl. After placing the cap on the bottle, the mixture was vigorously stirred. The uniformly dispersed mixture was irradiated under a 360 nm UV lamp

with an intensity of 500 mW/cm² for 1 hour. After irradiation, the Pd_1/TiO_2-L product was collected through centrifugation, washing, and drying. ICP analysis determined the Pd content in Pd_1/TiO_2-L to be 0.35 wt.%. The nitrogen content of the Pd_1/TiO_2 -L sample was quantified using an oxygen/nitrogen/hydrogen elemental analyzer (LECO ONH836) and determined to be 0.23 wt%. The synthesis of Pd_1/TiO_2-S, Pt_1/TiO_2-S, and Rh_1/TiO_2-S followed the same procedure, with Pd_{NPs}/TiO_2-S, Pt_{NPs}/TiO_2-S, and Rh_{NPs}/TiO_2-S replacing Pd_{NPs}/TiO_2-L as the precursors, respectively.

Synthesis of $Pd_1/C\&TiO_2$(Comm.)

8.3 mg of Comm.Pd/C and 100 mg of TiO_2-S were dispersed in 40 mL of CH_3CN and placed in a quartz bottle, followed by the addition of 2 μL of HCl. After placing the cap on the bottle, the mixture was vigorously stirred. The uniformly dispersed mixture was irradiated under a 360 nm UV lamp with an intensity of 50 mW/cm² for 0.5 hour. After irradiation, the $Pd_1/C\&TiO_2$(Comm.) product was collected through centrifugation, washing, and drying. ICP analysis determined the Pd content in $Pd_1/C\&TiO_2$(Comm.) to be 0.378 wt.%.

Synthesis of $Pd_1/C\&TiO_2$(Ind.W.)

4.0 mg of Ind.W.Pd/C and 100 mg of TiO_2-S were dispersed in 40 mL of CH3CN and placed in a quartz bottle, followed by the addition of 2 μL of HCl. After placing the cap on the bottle, the mixture was vigorously stirred. The uniformly dispersed mixture was irradiated under a 360 nm UV lamp with an intensity of 50 mW/cm² for 1 hour. After irradiation, the $Pd_1/C\&TiO_2$(Ind.W.) product was collected through centrifugation, washing, and drying. ICP analysis determined the Pd content in $Pd_1/C\&TiO_2$(Ind.W.) to be 0.370 wt.%.

EPR

EPR measurements were performed using a Bruker A300 spectrometer. The instrument was operated at a center field of 3510.0 G, sweep width of 100.0 G, microwave frequency of 9.853 GHz, microwave power of 19.72 mW, modulation frequency of 100.0 kHz, modulation amplitude of 1.0 G, time constant of 10.24 ms, and sweep time of 46.08 s. For the detection of chlorine radicals (•Cl), 50 mg of Pd_{NPs}/TiO_2 was dispersed in 20 mL of a CH_3CN/HCl solution (1 μL HCl), and 100 μL of the dispersion was mixed with 100 μL of 100 mM PBN solution. A 60 μL aliquot of the resulting mixture was loaded into a capillary and analyzed using in situ EPR under UV irradiation at 0, 1, and 10 minutes. For the detection of superoxide radicals ($\bullet O_2^-$) and alkyl radicals ($\bullet CH_2CN$), the same dispersion protocol was used, and 100 μL of the catalyst suspension was mixed with 100 μL of 100 mM DMPO solution. A 60 μL sample was loaded into a capillary and analyzed using in situ EPR under UV irradiation at 0, 1, and 10 minutes.

Catalytic tests

The catalyst, $Pd_1/C\&TiO_2$(Comm.), was first dispersed in ethanol. Certain amount of the dispersion was taken for catalytic reaction, depended on the amount of catalyst needed. To be specific, for styrene hydrogenation with a mole ratio of 1.5:10000 (Pd:styrene), 7.5×10^{-3} μmol Pd was needed. After the taken dispersion of $Pd_1/C\&TiO_2$(Comm.) was diluted in 10 mL ethanol in a glass pressure vessel, the catalyst dispersion was then sonicated and mixed with 50 μmol styrene by a magnetic stirring bar. The vessel was then charged with H_2 to 1 atm pressure and kept at 30 ℃ in a oil bath during stirring. The reaction progress and conversion were monitored using gas chromatographic analysis. For the other catalysts [i.e, TiO_2, Comm.Pd/C, Ind.W.Pd/C

and $Pd_1/C\&TiO_2$(Ind.W.)], they were also dispersed in ethanol for catalysis. The reaction conditions were kept the same with that for $Pd_1/C\&TiO_2$(Comm.). Catalytic activity data were obtained from three independent experiments under identical conditions, and the average values were reported.

Metal dispersion determination

The metal dispersion was determined for turn over frequency (TOF) calculations by CO titration experiments. The CO titration experiments were carried out on a Micromeritics Auto Chem II 2920 chemical adsorption instrument with TCD detector.

DFT calculations

First-principles calculations based on density functional theory (DFT) were performed using the Vienna Ab initio Simulation Package (VASP.6.1.2)[44]. The exchange-correlation energy was described within the generalized gradient approximation (GGA) with the Perdew-Burke-Ernzerhof (PBE) functional[45]. The projector augmented wave (PAW) method was employed in combination with a plane-wave basis set[46], with a cutoff energy of 400 eV. Convergence criteria were set to 1×10^{-4} eV for the total energy and 5×10^{-2} eV/Å for the atomic forces. All calculations were carried out in a solvent environment, where the acetonitrile electrolyte (relative permittivity $\varepsilon = 37.5$) was implicitly modeled using the polarizable dielectric continuum model implemented in the VASPsol code[47]. The TiO_2 support was modeled using an anatase TiO_2 (101) slab constructed from the bulk structure and expanded to a 3 × 4 surface supercell (cell parameters: a = 16.3287 Å, b = 18.8800 Å, c = 25.3775 Å). The slab consists of three TiO_2 layers. To eliminate spurious interactions between periodic slab images, a 15 Å

vacuum layer was introduced along the z-direction. During geometry optimization, the topmost TiO_2 layer was fully relaxed, while the bottom two layers were kept fixed at their bulk positions to mimic a semi-infinite substrate. All adsorbates and Pd species were fully optimized together with the relaxed surface layer[48]. Additionally, dipole moment correction was applied in all surface structure optimizations to suppress artificial electric fields arising from the asymmetric slab-vacuum configuration[49]. Brillouin zone sampling was performed using the Monkhorst-Pack scheme, with k-point grids generated by VASPkit[50] following a recommended spacing of 0.04 × 2π $Å^{-1}$. van der Waals interactions were accounted for using the DFT-D3 dispersion correction method[51].

The adsorption energy (E_{ad}) was calculated to evaluate the stability of adsorbed species, following the formula:

$$E_{ad} = E_{total} - E_{slab} - E(M) \quad (5)$$

where E_{total} denotes the total energy of the slab-adsorbate system, E_{slab} is the energy of the clean slab, and E(M) represents the energy of the molecule (M).

Reaction free energies (ΔG) were computed by considering the enthalpic and entropic contributions at 298.15 K and 1 atm, using the relation:

$$\Delta G = \Delta E_{DFT} + \Delta E_{zpe} - T\Delta S \quad (6)$$

where E_{DFT} is the total energy obtained from DFT calculations, E_{zpe} denotes the zero-point vibrational energy (derived from harmonic frequency analysis), The entropy of adsorbed

molecules ($T\Delta S$) is calculated from the vibrational frequencies associated with the normal modes in the harmonic approximation.

Data availability

Source data are provided with this paper. All data are available from the corresponding author upon request.

References

1. Zhu, C., Du, D., Eychmueller, A. & Lin, Y. Engineering Ordered and Nonordered Porous Noble Metal Nanostructures: Synthesis, Assembly, and Their Applications in Electrochemistry. *Chem. Rev.* **115**, 8896-8943 (2015).
2. Liu, X. et al. Noble metal-metal oxide nanohybrids with tailored nanostructures for efficient solar energy conversion, photocatalysis and environmental remediation. *Energy Environ. Sci.* **10**, 402-434 (2017).
3. Fuerstner, A. Gold and platinum catalysis-a convenient tool for generating molecular complexity. *Chem. Soc. Rev.* **38**, 3208-3221 (2009).
4. Zhang, S. et al. Catalysis on singly dispersed bimetallic sites. *Nat. Commun.* **6**, 7938 (2015).
5. Xu, Z. et al. Size-dependent catalytic activity of supported metal clusters. *Nature* **372**, 346-348 (1994).
6. Sehested, J., Gelten, J.A.P., Remediakis, I.N., Bengaard, H. & Nørskov, J.K. Sintering of nickel steam-reforming catalysts: effects of temperature and steam and hydrogen pressures. *J. Catal.* **223**, 432-443 (2004).
7. Corma, A. et al. Exceptional oxidation activity with size-controlled supported gold clusters of low atomicity. *Nat. Chem.* **5**, 775-781 (2013).
8. Wang, X., Zhuang, J., Peng, Q. & Li, Y. A general strategy for nanocrystal synthesis. *Nature* **437**, 121-124 (2005).

9. Qiao, B. et al. Single-atom catalysis of CO oxidation using Pt_1/FeO_x. *Nat. Chem.* **3**, 634-641 (2011).

10. Wu, Y., Wang, D. & Li, Y. Understanding of the major reactions in solution synthesis of functional nanomaterials. *Sci. China Mater.* **59**, 938-996 (2016).

11. Thomas, J.M. Tens of thousands of atoms replaced by one. *Nature* **525**, 325-326 (2015).

12. Yin, P. et al. Single Cobalt Atoms with Precise N-Coordination as Superior Oxygen Reduction Reaction Catalysts. *Angew. Chem. Int. Ed.* **55**, 10800-10805 (2016).

13. Guo, X. et al. Direct, Nonoxidative Conversion of Methane to Ethylene, Aromatics, and Hydrogen. *Science* **344**, 616-619 (2014).

14. Yang, X.-F. et al. Single-Atom Catalysts: A New Frontier in Heterogeneous Catalysis. *Acc. Chem. Res.* **46**, 1740-1748 (2013).

15. Campbell, C.T., Parker, S.C. & Starr, D.E. The Effect of Size-Dependent Nanoparticle Energetics on Catalyst Sintering. *Science* **298**, 811-814 (2002).

16. Asoro, M.A., Kovar, D., Shao-Horn, Y., Allard, L.F. & Ferreira, P.J. Coalescence and sintering of Pt nanoparticles:in situobservation by aberration-corrected HAADF STEM. *Nanotechnology* **21**, 025701 (2010).

17. Simonsen, S.B. et al. Direct Observations of Oxygen-induced Platinum Nanoparticle Ripening Studied by In Situ TEM. *J. Am. Chem. Soc.* **132**, 7968-7975 (2010).

18. Hansen, T.W., DeLaRiva, A.T., Challa, S.R. & Datye, A.K. Sintering of Catalytic Nanoparticles: Particle Migration or Ostwald Ripening? *Acc. Chem. Res.* **46**, 1720-1730 (2013).

19. Risse, T., Shaikhutdinov, S., Nilius, N., Sterrer, M. & Freund, H.-J. Gold Supported on Thin Oxide Films: From Single Atoms to Nanoparticles. *Acc. Chem. Res.* **41**, 949-956 (2008).

20. Datye, A.K., Xu, Q., Kharas, K.C. & McCarty, J.M. Particle size distributions in heterogeneous catalysts: What do they tell us about the sintering mechanism? *Catal. Today* **111**, 59-67 (2006).

21. Jones, J. et al. Thermally stable single-atom platinum-on-ceria catalysts via atom trapping. *Science* **353**, 150-154 (2016).
22. Wei, S. et al. Direct observation of noble metal nanoparticles transforming to thermally stable single atoms. *Nat. Nanotechnol.* **13**, 856-861 (2018).
23. Feng, S. et al. In situ formation of mononuclear complexes by reaction-induced atomic dispersion of supported noble metal nanoparticles. *Nat. Commun.* **10**, 5281 (2019).
24. Wang, S. et al. Ligand Assisted Thermal Atomization of Palladium Clusters: An Inspiring Approach for the Rational Design of Atomically Dispersed Metal Catalysts. *Angew. Chem. Int. Ed.* **62**, e202218630 (2023).
25. Luo, S. et al. Light-Induced Dynamic Restructuring of Cu Active Sites on TiO_2 for Low-Temperature H_2 Production from Methanol and Water. *J. Am. Chem. Soc.* **145**, 20530-20538 (2023).
26. Kaichev, V.V. et al. High-Pressure Studies of CO Adsorption on Pd(111) by X-ray Photoelectron Spectroscopy and Sum-Frequency Generation. *J. Phys. Chem. B* **107**, 3522-3527 (2003).
27. Wang, H. et al. Quasi Pd_1Ni single-atom surface alloy catalyst enables hydrogenation of nitriles to secondary amines. *Nat. Commun.* **10**, 4998 (2019).
28. Giannakakis, G. et al. Single-Atom Alloy Formation via Reaction-Driven Catalyst Restructuring. *J. Am. Chem. Soc.* **146**, 20989-20995 (2024).
29. Zhang, W. et al. High-performance photocatalytic nonoxidative conversion of methane to ethane and hydrogen by heteroatoms-engineered TiO_2. *Nat. Commun.* **13**, 2806 (2022).
30. Ding, S. et al. Electrostatic Stabilization of Single-Atom Catalysts by Ionic Liquids. *Chem* **5**, 3207-3219 (2019).
31. Ge, X. et al. Palladium Single Atoms on TiO_2 as a Photocatalytic Sensing Platform for Analyzing the Organophosphorus Pesticide Chlorpyrifos. *Angew. Chem.* **132**, 238-242 (2019).
32. Li, X. et al. Cooperative catalysis by a single-atom enzyme-metal complex. *Nat.*

Commun. **13**, 2189 (2022).

33. Lu, Y. et al. Enhancing Activity and Stability of Pd-on-TiO_2 Single-Atom Catalyst for Low-Temperature CO Oxidation through in Situ Local Environment Tailoring. *J. Am. Chem. Soc.* **146**, 28141-28152 (2024).
34. Dahl, M., Liu, Y. & Yin, Y. Composite Titanium Dioxide Nanomaterials. *Chem. Rev.* **114**, 9853-9889 (2014).
35. Shang, H. et al. Scalable and selective gold recovery from end-of-life electronics. *Nat. Chem. Eng.* **1**, 170-179 (2024).
36. Chen, Y. et al. Selective recovery of precious metals through photocatalysis. *Nat. Sustain.* **4**, 618-626 (2021).
37. Zhang, Y. et al. Efficient ammonia removal and toxic chlorate control by using $BiVO_4/WO_3$ heterojunction photoanode in a self-driven PEC-chlorine system. *J. Hazard. Mater.* **402**, 123725 (2021).
38. Ding, A. et al. Recovering palladium and gold by peroxydisulfate-based advanced oxidation process. *Sci. Adv.* **10**, eadm9311 (2024).
39. Liu, P. et al. Photochemical route for synthesizing atomically dispersed palladium catalysts. *Science* **352**, 797-800 (2016).
40. Chen, X. et al. Photocatalytic Free Radical-Controlled Synthesis of High-Performance Single-Atom Catalysts. *Angew. Chem. Int. Ed.* **62**, e202312734 (2023).
41. Ye, X. et al. Insight of the stability and activity of platinum single atoms on ceria. *Nano Research* **12**, 1401-1409 (2019).
42. Matsubu, J.C., Yang, V.N. & Christopher, P. Isolated Metal Active Site Concentration and Stability Control Catalytic CO_2 Reduction Selectivity. *J. Am. Chem. Soc.* **137**, 3076-3084 (2015).
43. Liu, B. et al. Molecular Understanding of Heterogeneous Hydroformylation on Rh_1/CeO_2: Morphology Effects. *ACS Catalysis.* **14**, 15956-15964 (2024).
44. Kresse, G. & Furthmüller, J. Efficient iterative schemes for ab initio total-energy

calculations using a plane-wave basis set. *Phys. Rev. B.* **54**, 11169-11186 (1996).

45. Perdew, J. P., Burke, K. & Ernzerhof, M. Generalized gradient approximation made simple. *Phys. Rev. Lett.* **77**, 3865-3868 (1996).
46. Kresse, G. & Joubert, D. From ultrasoft pseudopotentials to the projector augmented-wave method. *Phys. Rev. B.* **59**, 1758-1775 (1999).
47. Mathew, K. et al. Implicit solvation model for density-functional study of nanocrystal surfaces and reaction pathways. *J. Chem. Phys.* **140**, 084106 (2014).
48. Luo, Z., Wang, Z., Li, J., Yang, K. & Zhou, G. N-Promoted Ru_1/TiO_2 single-atom catalysts for photocatalytic water splitting for hydrogen production: a density functional theory study. *Phys. Chem. Chem. Phys.* **22**, 11392-11399 (2020).
49. Bengtsson, L. Dipole correction for surface supercell calculations. *Phys. Rev. B.* **59**, 12301-12304 (1999).
50. Wang, V. et al. VASPKIT:A user-friendly interface facilitating high-throughput computing and analysis using VASP code. Comput. *Phys. Commun.* **267**, 108033 (2021).
51. Grimme, S. et al. A consistent and accurate ab initio parametrization of density functional dispersion correction (DFT-D) for the 94 elements H-Pu. *J. Chem. Phys.* **132**, 154104 (2010).

Acknowledgements

This work was supported by the National Natural Science Foundation of China (22525606, 22176128, 22236005), the Innovation Program of Shanghai Municipal Education Commission (2023ZKZD50), Shanghai Leading Talent Program of Eastern Talent Plan (LJ2023002), Chinese Education Ministry Key Laboratory and International Joint Laboratory on Resource Chemistry, and Shanghai Eastern Scholar Program. “111 Innovation and Talent Recruitment Base on Photochemical and Energy Materials” (No. D18020), Yunnan University Collaborative

Innovation Center (Qujing Green Photovoltaic Industry Collaborative Innovation Center), Technology Talent and Platform Plan Project of Yunnan Provincial Department of Science and Technology (202305AF150088), Shanghai Engineering Research Center of Green Energy Chemical Engineering (18DZ2254200). Shanghai Frontiers Science Center of Biomimetic Catalysis.

Author contributions

X.C. and Z.B. proposed the study. X.C. conceived the research, designed the experiments, characterized the samples and drafted the manuscript. X.C. and K.Z. performed the DFT simulations. Z.B. and X.Q. conceived the research and designed the experiments. Q.Z. and X.Q. was responsible for the STEM characterization. J.Z. and K.Z. conceived the research and performed catalytic evaluation. All the authors discussed the results and participated in writing the manuscript.

Competing interests

The authors declare no competing interests.

Corresponding authors

Correspondence to Zhenfeng Bian and Xufang Qian.

Additional Information

Supplementary Information is available for this paper.

Correspondence and requests for materials should be addressed to Zhenfeng Bian. (bianzhenfeng@shnu.edu.cn) and Xufang Qian. (qianxufang@sjtu.edu.cn).

Editorial summary:

Converting metal nanoparticles into single-atom catalysts remains a challenge. This light-driven method uses chlorine radicals to disperse noble metals at room temperature, dramatically boosting the activity of industrial catalysts.

Peer Review Information: *Nature Communications* thanks Xiaoqiang An, Andrew Logsdail, who co-reviewed with Igor Kowalec, and the other, anonymous, reviewer(s) for their contribution to the peer review of this work. A peer review file is available.